Supporting Information

Exploring the Performance and Mass Transfer Characteristics of Porous Zinc Anodes for Membraneless Hybrid Flow Batteries

Lina Tang[1,+], Shuyang Dai[1,+], Puiki Leung[1,*], Mohd Rusllim Mohamed[2], Yikai Zeng[3,*], Xun Zhu[1], Cristina Flox[4], Akeel A. Shah[1], and Qiang Liao[1]

[1]Key Laboratory of Low-grade Energy Utilization Technologies and Systems, MOE, Chongqing University, Chongqing, 400030, China; 20211001017@cqu.edu.cn (L.T.); 20201001044@cqu.edu.cn (S.D.); zhuxun@cqu.edu.cn (X.Z.); akeel-shah@cqu.edu.cn (A.A.S.); lqzx@cqu.edu.cn (Q.L.)

[2]Faculty of Electrical and Electronics Engineering Technology, Universiti Malaysia Pahang, Pekan 26600, Malaysia; rusllim@ump.edu.my

[3]Institute of Engineering Thermophysics and New Energy, School of Mechanical Engineering, Southwest Jiaotong University, Chengdu, 610032, China

[4]Institut de Ciencia de Materials de Barcelona, CSIC, Campus UAB, Barcelona, 08193, Spain; cflox@icmab.es

* Correspondence: P.leung@cqu.edu.cn (P.L.); ykzeng@swjtu.edu.cn (Y.Z.)

[+] These authors have contributed equally to this work.

1. Main equations involved in the analysis of experimental data

The mean crystallite size (d) in nanometers (nm) was determined using the Scherrer equation (1), which takes into account the dimensionless shape factor (K = 0.94), diffraction wavelength (λ = 0.15406 nm), full width at half maximum (β) in radians, and Bragg angle (θ) in radians. Assuming spherical crystals with cubic symmetry and Gaussian peak profiles, the (002) lattice planes of Zn plate, Zn mesh, Zn foam, and Zn fiber were found to have mean crystallite sizes of 0.123 nm, 0.040 nm, 0.039 nm, and 0.038 nm, respectively.

$$d = \frac{K\lambda}{\beta \cos\theta} \tag{1}$$

According to the thermodynamic model of the Gibbs–Thomson melting point reduction（Equation (2)）, the average particle size of the zinc mesh, zinc foam, and zinc fiber is 0.154 nm, 0.135 nm, and 0.103 nm, respectively.

$$d = \frac{4\gamma_{sl}}{H_f \rho_s (1 - (\frac{T_M(porous)}{T_{MP}}))} \tag{2}$$

The melting temperature in Kelvin (K) was read at the onset of the endothermic phase transition based on the DSC patterns for different zinc materials. Here, T_{MP} and T_M (porous) are the zinc plate melting temperature and porous zinc melting temperature, respectively. The zinc plate heat of fusion (H_f) in Joules per gram (J g^{-1}) was calculated by analyzing endothermic peak in the

time–heat flow pattern (Figure S2, Hf = 86.157 J g^{-1}). Moreover, solid–liquid interfacial energy (γ_{sl}) in Joules per square meter (J m^{-2}, γsl (Zn)=110 mJ m^{-2}), density of the solid (ρ_s) in grams per cubic meter (g m^{-3}) (ρs (Zn)=7.14×10^6 g m^{-3}), and the onset of the endothermic phase transition were calculated. The physical constants were obtained from relevant literature sources [1,2].

The Butler–Volmer equation was employed to calculate the kinetic parameters of zinc in regions where electron transfer is limited. The Butler–Volmer relationship is expressed by Equation (3), in which j_0 represents the exchange current, η is the activation overpotential, and α_c is the cathodic charge transfer coefficient. The measured Tafel plots and Butler–Volmer fits for various Zn electrodes are presented in Figure 4c, and the calculated kinetic parameters for different potentials are provided in Table S2.

$$j = j_0 \left\{ \exp\left[\frac{(1-\alpha_c) nF\eta}{RT} \right] - \exp\left[-\frac{\alpha_c nF\eta}{RT} \right] \right\} \tag{3}$$

2. Model geometry and assumptions

The models investigated in this work comprised negative zinc electrodes (including zinc plates, zinc fibers, zinc meshes, and zinc foams), positive carbon electrodes, and internal flow channels (as shown in Figure S1a for a schematic representation of the three-dimensional model of a zinc plate electrode battery and Figure S1b for a zinc fiber electrode battery). The thickness of the deposited metal zinc was assumed to be negligible in relation to the inter-electrode distance, providing a reasonable approximation. The zinc mesh and zinc foam batteries shared the same overall structure, with the only difference being the structure of their respective zinc electrodes. For all simulations, the electrolyte was assumed to be an incompressible fluid with uniform texture and viscosity and negligible side reactions. The electrolyte solution was pumped from external liquid storage tanks into the batteries during charging, although the effects of pipelines and pumps were neglected, and instead, Global ODEs and DAEs interfaces were used to model the system. During the charge process, divalent zinc ions (Zn^{2+}) gained electrons from the negative electrode, reducing to zinc metal and depositing on the negative electrode collector. At the positive electrode, hydroquinone (HQ) was oxidized, losing electrons to form p-benzoquinone (BQ). The discharge reaction was simply the reverse of the charging reaction.

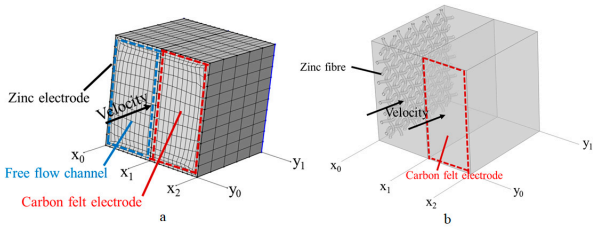

Figure S1. Schematic of three-dimensional hybrid flow batteries models: (**a**) zinc plate electrode battery; (**b**) zinc fiber electrode battery.

2.1. Conservation of charge

It is assumed that the electrolyte satisfies electroneutrality; i.e., $\sum_i z_i c_i = 0$, and the sum of the positive and negative ion concentrations in the electrolyte is equal to zero. From the conservation of charge, the charge $\boldsymbol{i}_l$ that enters the electrolyte must match the charge $\boldsymbol{i}_s$ that leaves the solid phase, which demands that the sum of the charges of the positive and negative ions is equal to the charge of the electrons transferred through the electrochemical reaction $\nabla \cdot \boldsymbol{i}_l + \nabla \cdot \boldsymbol{i}_s = 0$. The total current transferred from the solid phase to the electrolyte phase is given by $\nabla \cdot \boldsymbol{i} = \nabla \cdot \boldsymbol{i}_l = -\nabla \cdot \boldsymbol{i}_s$. It shall equal the net volumetric rate of electrochemical reaction multiplied by Faraday's constant *F*. The charged species flow with given fluxes through the electrolyte at a pseudo-steady state, which generates a current flow. By exploiting electroneutrality, the following relationship can be derived:

$$\boldsymbol{i}_l = -\sigma_l \nabla\phi - F \sum_i z_i D_i \nabla c_i \tag{4}$$

in which $\sigma_l = F^2 \sum_i z_i^2 D_i \nabla c_i / (RT)$ is the electrolyte conductivity. In the porous electrode, the conductivity is Bruggeman corrected to obtain $\sigma_l^{eff} = \epsilon^{3/2} \sigma_l$. Ohm's law is used to govern the solid-state potential ϕ_s:

$$-\sigma_s^{eff}\nabla^2\phi_s = -\nabla\cdot\boldsymbol{i} \quad (5)$$

in which $\sigma_s^{eff} = (1-\epsilon^{3/2})\sigma_s$ is the Bruggeman-corrected conductivity (pure value σ_s).

2.2. Electrochemical reactions

The electrochemical reactions occurring at the electrodes are assumed to follow the Butler–Volmer equation, as represented by Equations (6) and (7) for the positive and negative electrode reactions, respectively.

$$\nabla\cdot\boldsymbol{i} = AFk_{pos}\left(a_{HQ}\right)^{\alpha_{pos}}\left(a_{PQ}\right)^{1-\alpha_{pos}}\left[exp\left(\frac{(1-\alpha_{pos})nF\eta_{pos}}{RT}\right) - exp\left(-\frac{\alpha_{pos}F\eta_{pos}}{RT}\right)\right] \quad (6)$$

$$\nabla\cdot\boldsymbol{i} = Fk_{neg}\left(a_{Zn(II)}\right)^{1-\alpha_{neg}}\left[exp\left(\frac{(1-\alpha_{neg})nF\eta_{neg}}{RT}\right) - exp\left(-\frac{\alpha_{neg}F\eta_{neg}}{RT}\right)\right] \quad (7)$$

Here, k_{pos} and k_{neg} are the reaction rate constants for the positive and negative electrode reactions, while a_i is the activity of species *i*, and *n* is the number of electrons transferred in the reaction. Additionally, α_{pos} and α_{neg} are the charge transfer coefficients, and η_{pos} and η_{neg} are the overpotentials, which are in the form of $\eta = \phi_s - \phi_l - E_{eq}$, where E_{eq} is the equilibrium potential of the reaction. The equilibrium potential is given by the Nernst equation at both the positive and negative electrodes:

$$E_{eq}^{pos} = E_0^{pos} + \frac{RT}{nF}ln\left(\frac{(c_{PQ})(c_H)^2}{c_{HQ}}\right) \quad (8)$$

$$E_{eq}^{neg} = E_0^{neg} + \frac{RT}{nF}lnc_{z_n(II)} \quad (9)$$

Here, E_0^{pos} and E_0^{neg} are the standard potentials of the positive and negative electrodes, respectively.

2.3. Conservation of Mass and fluid flow

During the charge and discharge processes, the electrolyte consisting of zinc chloride and quinone species undergoes a chemical transformation, producing Cl^-, H^+, Zn^{2+}, BQ, and HQ. These species are conserved, and their fluxes are assumed to follow the Nernst–Planck equation in both the free channel and porous electrode, which are represented, respectively, by Equations (10) and (11).

$$\frac{\partial c_i}{\partial t} + \nabla\cdot\left(-D_i\nabla c_i - \frac{z_i c_i D_i}{RT}F\nabla\phi + \mathbf{u}c_i\right) = 0 \quad (10)$$

$$\frac{\partial(\epsilon c_i)}{\partial t} + \nabla\cdot\left(-D_i^{eff}\nabla c_i - \frac{z_i c_i D_i^{eff}}{RT}F\nabla\phi + \mathbf{u}_{eff}c_i\right) = \frac{Av_i\boldsymbol{i}}{2F} \quad (11)$$

The electrode porosity ε, molar gas constant R, electrolyte temperature T, and Faraday constant F are considered in these equations. The concentration, diffusion coefficient, and valence state of species i are denoted by c_i, D_i, and z_i, respectively. ϕ, $\mathbf{u}$, and $\mathbf{u_{eff}}$ are the ionic potential, electrolyte flow rate, and effective electrolyte flow rate; A is the specific surface area for reaction; v_i is the stoichiometric coefficient of species *i* in reactions (5); and $\boldsymbol{i}$ is the total current. The effective diffusion coefficient $D_i^{eff} = \epsilon^{3/2}D_i$ is obtained by Bruggeman correction in the porous electrode. In the porous electrode, the flow velocity follows Brinkman's equation (12):

$$\nabla p = -\frac{\mu}{\kappa}\epsilon\mathbf{u}_{eff} + \mu\nabla^2\mathbf{u}_{eff} \quad (12)$$

where p is the liquid pressure, κ is the electrode permeability, and μ is the dynamic viscosity. The continuity and incompressible Navier–Stokes equations are assumed to govern the electrolyte flow rate $\mathbf{u}$ in the channel and the pressure p.

$$\rho\frac{\partial\boldsymbol{u}}{\partial t} + \rho(\mathbf{u}\cdot\nabla)\mathbf{u} = -\nabla p + \mu\nabla^2\mathbf{u} \quad (13)$$

$$\nabla\cdot\mathbf{u} = 0 \quad (14)$$

2.4. Boundary conditions

The boundary conditions are specified in Figure S1. At x_0 and x_2, the mass flux is assumed to be zero, as is the flux of electrons at y_0 and y_1. The external boundary is subject to a Neumann boundary condition for the pressure except at the inlet and exit as $\nabla p\cdot\boldsymbol{n} = \mathbf{0}$, where the electrolyte enters at the inlet with a specified flow rate and concentration due to the continuous pump

action, resulting in $\mathbf{u} = (0, U_{in})$ and $c = c_i^{in}$. The diffusive fluxes for all species are assumed to be zero at the outlet as $-D_i \nabla c_i \cdot \boldsymbol{n} = 0$, where the unit normal is represented by $\boldsymbol{n}$. The outlet pressure condition is $p = p_{out}$.

Upon charging and discharging the battery, the negative electrode is maintained at a ground state, while the positive electrode voltage is set to the battery cell voltage. The electrolyte is pumped from the reservoir (of volume V_r) through the battery to absorb or release energy. This process affects the distribution of reactant concentrations and must be considered in the model. The volumetric flow rate Q of electrolyte at the outlet is given by $Q = U_{in} A_{out}$, where A_{out} represents the outlet cross-sectional area. The averaged concentrations at the outlet can be determined from the following:

$$c_i^{out} = \int c_i(x, y = h, t) dx \tag{15}$$

Assuming no reactions occur in the reservoir, and instantaneous mixing takes place, we obtain the following:

$$\frac{dc_i^{in}}{dt} = \frac{Q}{V_r}\left(c_i^{out} - c_i^{in}\right) \tag{16}$$

$$c_i^{in}(0) = c_i^0 \tag{17}$$

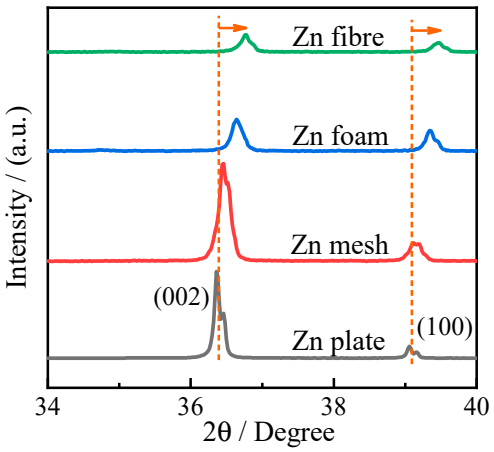

Figure S2. The local zoom-in X-ray powder diffraction patterns for different zinc materials.

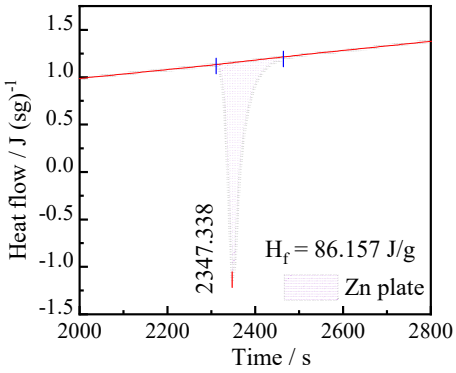

Figure S3. The time–heat flow pattern for zinc plate.

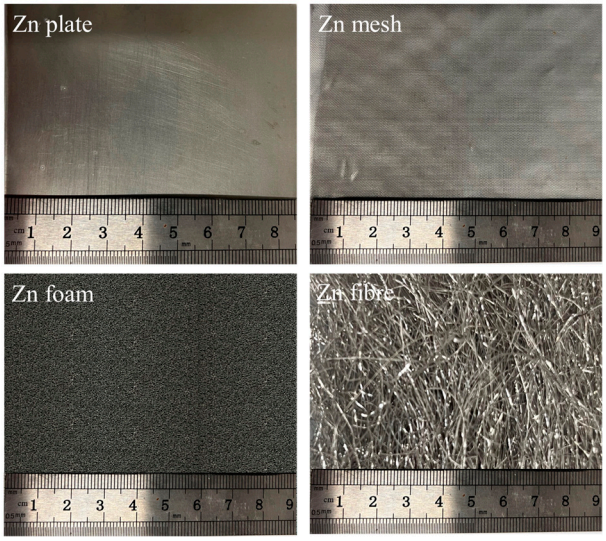

Figure S4. The optical images for different zinc electrodes.

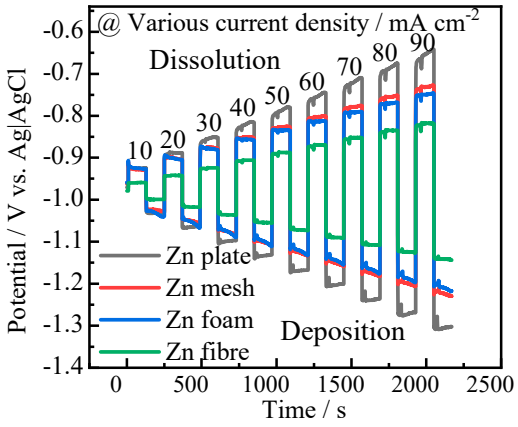

Figure S5. The short-time charging–discharging profiles to evaluate polarization potentials for different zinc electrodes.

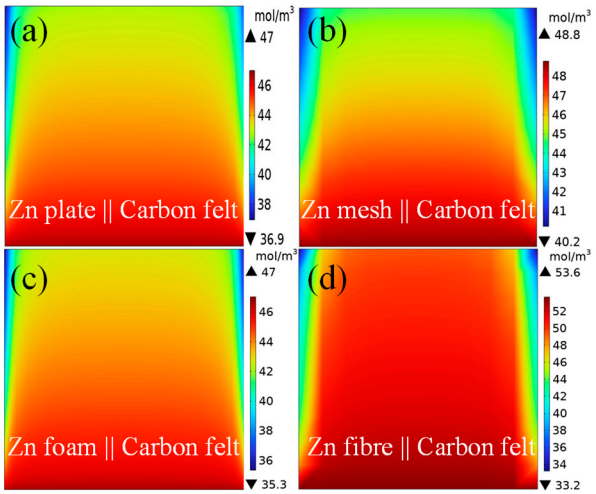

Figure S6. Concentration distribution of HQ at the interfaces between zinc electrodes and electrolyte solutions after 15 min charging (right view of cells).

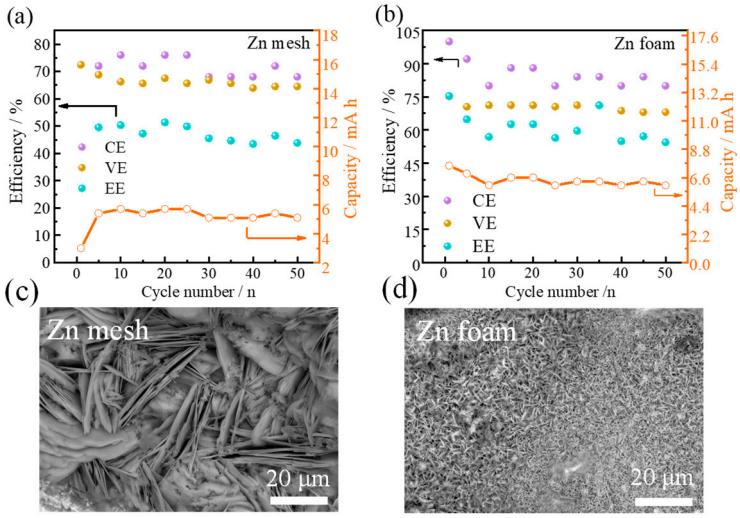

Figure S6. The time–heat flow pattern for zinc plate.

Figure S7. Comparison of the system efficiencies and capacities of the full batteries equipped with zinc mesh (**a**) and zinc foam anodes (**b**) at 30 mA cm^{-2}; the surface morphology of the zinc mesh anode (**c**) and zinc foam anode (**d**) after 100 cycles of charging–discharging.

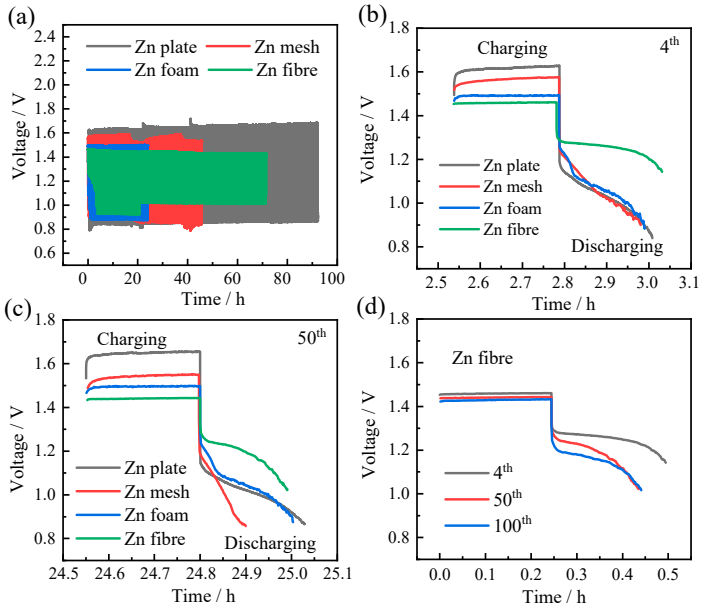

Figure S8. (**a**) Constant-current long-cycle charge–discharge curves; (**b**) charge–discharge profiles at the 4th cycle; (**c**) charge–discharge profiles at the 50th cycle for the full batteries equipped with zinc anodes; (**d**) charge–discharge profiles for the full batteries equipped with zinc fiber anode at the 4th, 50th, and 100th cycles, respectively.

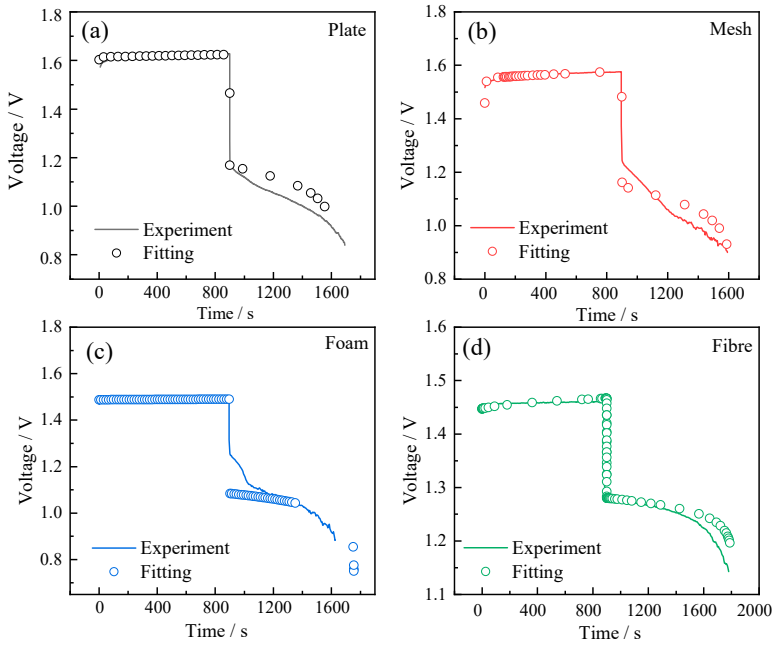

Figure S9. The validation of the COMSOL multiphysics model with experimental data. (a) Zinc plate, (b) zinc mesh, (c) zinc foam, and (d) zinc fiber.

Table S1. The calculation results of the mean crystallite size based on XRD (crystal plane (002)) and DSC for zinc materials.

Calculation results\2D/3D zinc	Zn plate	Zn mesh	Zn foam	Zn fiber
FWHM-XRD / °	0.155	0.200	0.202	0.208
d-XRD / nm	63.816	49.375	48.941	47.754
d-DSC / nm	——	154	135	103

Table S2. Measured kinetic parameters for 2D/3D zinc anodes from Butler–Volmer fit to Tafel slope.

2D/3D zinc anodes	Zn plate	Zn mesh	Zn foam	Zn fiber
j_0 / mA	44.7	58.9	63.1	83.2
Anodic Tafel slope / mV dec^{-1}	301.2	263.4	341.3	247.8
Cathodic Tafel slope / mVdec^{-1}	293.4	249.8	332.8	218.4

Table S3. The half-cell coulombic efficiencies at different states of charge for 2D/3D zinc anodes.

Zn\CE	0.25 h C-D	0.5 h C-D	1 h C-D	2 h C-D	3 h C-D
Zn plate	99.8%	99.9%	99.7%	99.6%	99.9%
Zn mesh	99.7%	99.6%	99.8%	99.8%	99.9%
Zn foam	99.5%	99.4%	99.2%	99.6%	99.3%
Zn fiber	99.3%	99.6%	99.5%	99.6%	99.6%

Table S4. The half-cell voltage efficiencies at different states of charge for 2D/3D zinc anodes.

Zn\VE	0.25 h C-D	0.5 h C-D	1 h C-D	2 h C-D	3 h C-D
Zn plate	69.1%	68.8%	69.3%	68.4%	70.5%
Zn mesh	80.6%	81.4%	81.2%	80.6%	80.5%
Zn foam	82.9%	82.8%	83.8%	83.3%	83.4%
Zn fiber	86.7%	88.2%	89.4%	90.2%	90.8%

Table S5. A summary of battery performance and capital cost for relevant aqueous conventional and zinc-based RFBs.

RFB systems	Cell Voltage / V	Capacity Retention / % per cycle	CE, EE / %	Cycle Number	Capital Cost / USD per kWh	Reference
All-V	1.4	99.95	85.90, 78.25	20	252	*Journal of Power Sources* 162 (2006) 1416–1420
Fe-Cr	1.0	99.40	97, 82	40	272	*Int J Energy Res.* 2019; 43:8739–8752.
Zn-Br	1.6	99.98	95, 81	100	436	*Electrochimica Acta* 388 (2021) 138451
Zn-Fe	1.2	99.82	95,78	60	412	*Surface and Coatings Technology* 358 (2019) 190-194
Zn-organics (HQ) membraneless	**1.1**	**99.88**	**90, 75**	**100**	**136**	**This work**

Reference

[S1] Jiang, Q. & Lu, H. M. Size dependent interface energy and its applications. Surf. Sci. Rep. 63, 427–464 (2008).

[S2] Roeber, E. F. & Parmelee, H. C. Electrochemical and Metallurgical Industry (Electrochemical Publishing Company, 1907).

[S3] F. Yu, A. Shah, P. Leung, A numerical model of a zinc-para-benzoquinone membrane-free organic flow battery, Energy Reports, 8 (2022) 1158-1165.